


## Evolution of ultraflat band in the van der Waals kagome semiconductor $\text{Pd}_3\text{P}_2(\text{S}_{1-x}\text{Se}_x)_8$

Shaohua Yan (闫少华)<sup>1,\*</sup>, Ben-Chao Gong (龚本超)<sup>1,\*</sup>, Lin Wang (王林)<sup>2</sup>, Jinzhi Wu (武晋治)<sup>1</sup>,  
Qiangwei Yin (殷蔷薇)<sup>1</sup>, Xinyu Cao (曹新宇)<sup>3</sup>, Xiao Zhang (张晓)<sup>3</sup>, Xiaofeng Liu (刘小峰)<sup>2,†</sup>, Zhong-Yi Lu (卢仲毅)<sup>1</sup>,  
Kai Liu (刘凯)<sup>1,‡</sup> and Hechang Lei (雷和畅)<sup>1,§</sup>

<sup>1</sup>*Department of Physics and Beijing Key Laboratory of Opto-electronic Functional Materials & Micro-nano Devices, Renmin University of China, Beijing 100872, China*

<sup>2</sup>*School of Materials Science & Engineering, Zhejiang University, Hangzhou 310027, China*

<sup>3</sup>*State Key Laboratory of Information Photonics and Optical Communications & School of Science, Beijing University of Posts and Telecommunications, Beijing 100876, China*

 (Received 22 November 2021; revised 11 March 2022; accepted 22 March 2022; published 8 April 2022)

We investigate the evolution of structural parameters, optical properties, and electronic structures of the van der Waals kagome semiconductor  $\text{Pd}_3\text{P}_2\text{S}_8$  with Se doping. When the doping level of Se increases, the band gaps of  $\text{Pd}_3\text{P}_2(\text{S}_{1-x}\text{Se}_x)_8$  single crystals decrease gradually, accompanied by the expanded unit cells. First-principles calculations show that there is a flat band (FB) near the Fermi level in bulk  $\text{Pd}_3\text{P}_2\text{S}_8$ . This FB mainly originates from the  $d_{z^2}$ -like orbitals of Pd atoms in the Pd kagome lattice, which has finite interlayer electron hopping perpendicular to the  $\text{PdS}_4$  square plane. The interlayer hopping can be reinforced with Se doping, inducing a stronger interlayer coupling via the chalcogen atoms at apical sites, which reduces the band gap and enhances the cleavage energy. In contrast, the vanishing interlayer hopping in the two-dimensional limit results in the formation of an ultra-FB in the monolayers of these compounds. The easy exfoliation and the existence of a unique ultra-FB near  $E_F$  make  $\text{Pd}_3\text{P}_2(\text{S}_{1-x}\text{Se}_x)_8$  a model system to explore the exotic physics of a FB in a two-dimensional kagome lattice.

DOI: [10.1103/PhysRevB.105.155115](https://doi.org/10.1103/PhysRevB.105.155115)

### I. INTRODUCTION

A flat band (FB) represents one type of unusual band structure with constant energy independent of the crystal momentum (dispersionless band in momentum space) [1–3]. The zero bandwidth (BW) of an ideal FB leads to a high density of states (DOS) and vanishing group velocity with an infinite effective mass of electrons. For quenched kinetic energy and a high DOS, FB systems are thought to have a strong, natural electron-electron correlation effect, which could result in several exotic many-body phenomena, such as ferromagnetism, superconductivity, Wigner crystals, etc. [4–9]. Moreover, when time-reversal symmetry is broken and spin-orbital coupling is considered, the FB can become topologically nontrivial with a nonzero Chern invariant, leading to a quantum Hall state or even a high-temperature fractional quantum Hall state [10,11]. In theory, various two-dimensional (2D) lattice models have been proposed to host the FB based on line-graph construction in general [4,12,13], such as dice, Lieb, kagome, and decorated square lattices, as well as a honeycomb lattice with multiple orbitals on each site [1,3,5,8,11–18].

The 2D kagome lattice composed of corner-sharing triangles and hexagons of atoms is one of the lattice models in which the FB exists [3]. This FB is rooted in the destructive

phase interference of electron hopping paths, and in real space the electronic state is geometrically confined within the single hexagon, forming a compact localized state [1,2]. Theoretical studies have shown that most exotic phenomena originating from the FB can appear in a kagome lattice [4,7,8,10,11]. Moreover, a 2D kagome lattice also exhibits a unique topological band structure and strong magnetic frustration effects such as a topologically nontrivial Dirac band, a saddle point with van Hove singularity, and a quantum spin liquid state [19–23]. Recent experimental studies on insulating or metallic materials with a 2D kagome lattice (kagome materials) have confirmed the existence of topological electronic structures including FBs [23–27], and they revealed various exotic phenomena-fractionalized excitations of the spin liquid state, negative FB magnetism, a large intrinsic anomalous Hall effect, a massive Dirac point with a Chern gap, a coexistent charge density wave and superconducting states, to name a few [28–37].

Despite their many fascinating properties, experimental studies on the intrinsic physical properties of kagome materials in a 2D limit, especially for FBs, are still scarce. Due to the finite interlayer couplings and the existence of structural layers other than the kagome one in real materials, the FB will be perturbed, inducing the band dispersion and hybridization with other bands [24–27]. Thus, in order to reveal the peculiar properties of a FB in a kagome lattice, the exploration of kagome materials with vanishing interlayer coupling becomes utterly important.

Recently, semiconducting  $\text{Pd}_3\text{P}_2\text{S}_8$  with a Pd kagome lattice was highlighted due to its weak van der Waals (vdW)

\*These authors contributed equally to this work.

†xfliu@zju.edu.cn

‡kliu@ruc.edu.cn

§hleil@ruc.edu.cn

interlayer interaction and a FB near  $E_F$  with a very small BW, closely related to the kagome structure of Pd atoms [38]. To understand the evolution and origin of this unusual FB in  $\text{Pd}_3\text{P}_2\text{S}_8$ , in this work we carry out a systematic study on  $\text{Pd}_3\text{P}_2(\text{S}_{1-x}\text{Se}_x)_8$  single crystals with  $x$  up to 0.25. It is found that with Se doping, the lattice parameters increase gradually but the band gaps decrease. Theoretical calculations indicate that the narrowing of the band gap and the increased cleavage energy can be ascribed to the enhanced interlayer coupling by Se doping. Further analysis reveals that the ultra-FB in monolayer  $\text{Pd}_3\text{P}_2\text{Ch}_8$  ( $\text{Ch} = \text{S}, \text{Se}$ ) originates from the Pd  $d_{z^2}$ -like orbitals of the Pd kagome lattice and the absence of interlayer electron hopping perpendicular to the local  $\text{PdCh}_4$  square plane.

## II. METHODS

Single crystals of  $\text{Pd}_3\text{P}_2(\text{S}_{1-x}\text{Se}_x)_8$  were grown by the chemical vapor transport method. Pd powder (99.98% purity), P powder (99.999% purity), S flakes (99.95% purity), and Se powder (99.99% purity) in a 3 : 2 : 8(1 -  $x$ ) : 8 $x$  molar ratio were put into a silicon tube with 80 mg iodine flakes (99.999%). The tube was sealed under high vacuum and then placed in a two-zone horizontal tube furnace. The temperatures of two zones were raised slowly to 993 and 963 K for 2 days and were then held there for another 3 days. After that, the temperatures were decreased slowly down to 673 and 623 K. Finally, the power of the furnace was switched off and the ampoule was cooled down naturally. Crystals with a typical size of  $3 \times 3 \times 0.5 \text{ mm}^3$  can be obtained.

The elemental analysis was performed using energy-dispersive x-ray spectroscopy (EDX). The doping level  $x$  mentioned below is the actual composition obtained from the EDX measurements. Exfoliation of  $\text{Pd}_3\text{P}_2(\text{S}_{1-x}\text{Se}_x)_8$  crystals was achieved using mechanical exfoliation with scotch tape and was transferred onto a 300-nm  $\text{SiO}_2$  covered Si substrate. The microscopy images were acquired using a Bruker Edge Dimension atomic force microscope (AFM). X-ray diffraction (XRD) patterns were measured using a Bruker D8 x-ray machine with Cu  $K\alpha$  ( $\lambda = 1.5418 \text{ \AA}$ ) radiation. Room-temperature optical transmission spectra of the samples were recorded in a Hitachi UH5700 spectrophotometer in the spectral range of 400–1100 nm. The exfoliated flakes of samples were fixed onto a stainless steel sample holder with an aperture diameter of 1.0 mm. The absorption coefficient ( $\alpha$ ) was then calculated according to the Beer-Lambert law.

Density functional theory (DFT) calculations on  $\text{Pd}_3\text{P}_2\text{Ch}_8$  ( $\text{Ch} = \text{S}, \text{Se}$ ) were performed with the projector augmented wave (PAW) method [39,40] as implemented in the Vienna Ab initio Simulation Package (VASP) [41–43]. The generalized gradient approximation (GGA) of Perdew-Burke-Ernzerhof (PBE) [44] type was adopted for the exchange-correlation functional. The kinetic energy cutoff of the plane-wave basis was set to 420 eV. A fully variable-cell relaxation was carried out to obtain the equilibrium lattice parameters. The internal atomic positions were relaxed with the quasi-Newton algorithm until the forces on all atoms were smaller than 0.01 eV/Å. For the Brillouin zone sampling of the bulk and the monolayer of  $\text{Pd}_3\text{P}_2\text{Ch}_8$ , the  $8 \times 8 \times 8$  and  $8 \times 8 \times 1$   $k$ -point meshes were used for the structural optimization

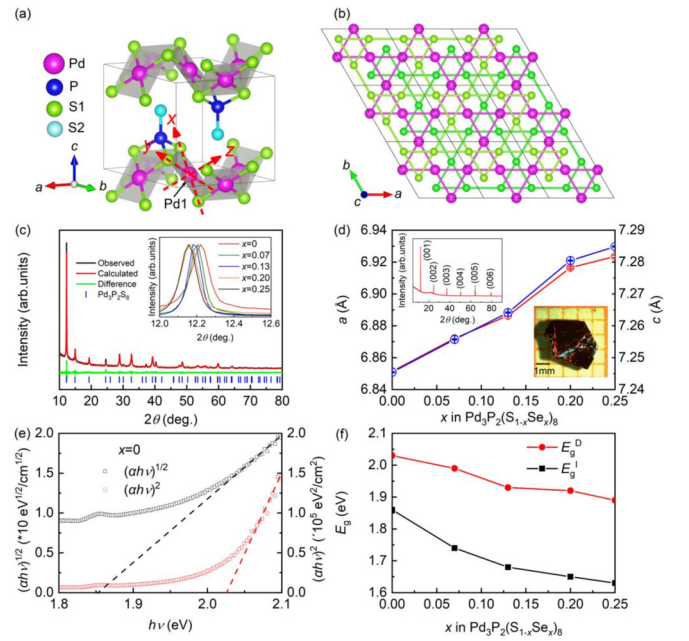


FIG. 1. (a) Crystal structure of  $\text{Pd}_3\text{P}_2\text{S}_8$ . The local Cartesian coordinates with the origin at the Pd1 atom are defined by the red arrows, where the  $z$ -axis is perpendicular to the  $\text{PdS}_4$  square plane. (b) Top view of Pd and S kagome layers. For clarity, the S1 atoms below and above the Pd layer are displayed in different colors. (c) Powder x-ray diffraction (XRD) pattern of  $\text{Pd}_3\text{P}_2\text{S}_8$ . Inset: (00 $l$ ) diffraction peaks for  $\text{Pd}_3\text{P}_2(\text{S}_{1-x}\text{Se}_x)_8$  with various  $x$ . (d) The  $a$ - and  $c$ -axial lattice parameters  $a$  and  $c$  as a function of  $x$ . Inset: left, XRD pattern; right, optical photo of a  $\text{Pd}_3\text{P}_2\text{S}_8$  single crystal. (e) The plots of  $(\alpha hv)^{1/2}$  and  $(\alpha hv)^2$  as a function of  $h\nu$  for  $\text{Pd}_3\text{P}_2\text{S}_8$  single crystal. (f) The estimated direct and indirect band gaps  $E_g^D$  and  $E_g^I$  of  $\text{Pd}_3\text{P}_2(\text{S}_{1-x}\text{Se}_x)_8$  single crystals with various  $x$ .

calculations, while the  $12 \times 12 \times 12$  and  $12 \times 12 \times 1$   $k$ -point meshes were used for the self-consistent calculations, respectively. The Gaussian smearing method with a width of 0.05 eV was utilized for the Fermi surface broadening. For the bulk  $\text{Pd}_3\text{P}_2\text{Ch}_8$ , the interlayer vdW interaction was described by using the DFT-D3 method of Grimme [45]. For the monolayer  $\text{Pd}_3\text{P}_2\text{Ch}_8$ , a vacuum space of 20 Å thickness was used to eliminate the interaction of periodic images. The DOS and total energies of the bulk crystals were obtained by using the tetrahedron method with Blöchl corrections [46].

## III. RESULTS AND DISCUSSION

$\text{Pd}_3\text{P}_2\text{S}_8$  has a layered structure with the stacking Pd-P-S blocking layers along the  $c$  axis [Fig. 1(a)]. The key structural ingredient is the perfect Pd kagome lattice in the Pd-P-S layer with the atomic distance of Pd atoms  $d_{\text{Pd-Pd}} \sim 3.418 \text{ \AA}$  [Fig. 1(b)] [47,48]. Below and above the Pd kagome layer, P and S atoms form  $\text{PS}_4$  tetrahedra, and each P atom occupies the center of a tetrahedron. As shown in Fig. 1(a), because of the inequivalent local environment of S atoms there are two S sites, and each of three S atoms at the S1 site in  $\text{PS}_4$  tetrahedra is coordinated with two Pd atoms and one P atom with  $d_{\text{Pd-S}} \sim 3.113 \text{ \AA}$  and  $d_{\text{P-S}} \sim 2.112 \text{ \AA}$ , when the fourth S atom at the S2 site is coordinated with one P atom only with

$d_{P-S} \sim 1.904 \text{ \AA}$ . Thus, the  $\text{PS}_4$  tetrahedron is distorted with the S-P-S angles deviating from  $109.47^\circ$  in an ideal tetrahedron to  $103.10^\circ$  and  $115.27^\circ$  [47,48]. More importantly, the vertical P-S bonds in two Pd-P-S layers protrude from each other, and it leads to the waved Pd-P-S layers and a unique interlocked layered structure of  $\text{Pd}_3\text{P}_2\text{S}_8$ , different from conventional vdW materials. In addition, in each Pd-P-S layer, the S atoms at the S1 site also form two distorted kagome lattices below and above the Pd kagome layer with two different values of  $d_{S-S}$  ( $\sim 3.176$  and  $3.665 \text{ \AA}$ ) [Fig. 1(b)]. On the other hand, each Pd atom is surrounded by four S atoms from two  $\text{PS}_4$  tetrahedra, forming a  $\text{PdS}_4$  tetragon that tilts away from the  $ab$  plane. To maintain electric neutrality, the oxidation state of Pd, P, and S in  $\text{Pd}_3\text{P}_2\text{S}_8$  is  $+2$ ,  $+5$ , and  $-2$ , respectively. The  $\text{Pd}^{2+}$  ion has an electronic configuration of  $[\text{Kr}]4d^8$ , which usually prefers to have a square-planar crystal field with a low spin state. This is consistent with the structural feature and diamagnetism of  $\text{Pd}_3\text{P}_2\text{S}_8$  [38].

Figure 1(c) shows the powder XRD pattern and Rietveld fit of ground  $\text{Pd}_3\text{P}_2\text{S}_8$  single crystals. The fitted  $a$ - and  $c$ -axial lattice parameters  $a$  and  $c$  are  $6.851(3)$  and  $7.246(5) \text{ \AA}$ , close to the previous results [47,48]. Powder XRD patterns of all Se-doped  $\text{Pd}_3\text{P}_2\text{S}_8$  samples can also be fitted very well by using the crystal structure of  $\text{Pd}_3\text{P}_2\text{S}_8$  with the trigonal symmetry (space group  $P-3m1$ , no. 164). Both fitted  $a$  and  $c$  increase with increasing Se content monotonically [Fig. 1(d)], which can be ascribed to the larger ionic radius of  $\text{Se}^{2-}$  than  $\text{S}^{2-}$ . The nearly linear trend of lattice expansion follows Vegard's law. Such increases of lattice parameters are also partially reflected by the shift of the peak position of (001) to a lower angle gradually with Se doping [inset of Fig. 1(c)]. It is noted that when  $x > 0.25$ , Se cannot be doped into the sample any further even if the nominal  $x$  reaches 0.5 and  $\text{Pd}(\text{S}, \text{Se})_2$  crystals start to grow. This suggests that the solubility limit of Se may be  $x = 0.25$ . The upper left inset of Fig. 1(d) shows the XRD pattern of a  $\text{Pd}_3\text{P}_2\text{S}_8$  single crystal. All of the peaks can be indexed by the indices of (00 $l$ ) lattice planes, indicating that the crystal surface is parallel to the  $ab$  plane and perpendicular to the  $c$  axis. The morphology of  $\text{Pd}_3\text{P}_2\text{S}_8$  single crystal is a thick plate with a hexagonal shape [lower right inset of Fig. 1(d)], consistent with the layered structure and the trigonal symmetry of  $\text{Pd}_3\text{P}_2\text{S}_8$ .

Optical transmittance spectra are measured to determine the band gaps of  $\text{Pd}_3\text{P}_2\text{S}_8$  using the Tauc plot method [50]. As shown in Fig. 1(e), the direct band gap  $E_g^D$  and the indirect one  $E_g^I$  can be estimated from the extrapolation of the linear region of  $(\alpha h\nu)^2$  and  $(\alpha h\nu)^{1/2}$  as a function of photon energy  $h\nu$  to zero. Here,  $\alpha$  is the absorption coefficient calculated from optical transmission spectra of the samples according to the Beer-Lambert law. The obtained values of  $E_g^D$  and  $E_g^I$  for  $\text{Pd}_3\text{P}_2\text{S}_8$  are 2.03 and 1.86 eV, in agreement with the values reported previously ( $E_g^D = 2.08 \text{ eV}$  and  $E_g^I = 1.85 \text{ eV}$ ) [38] and close to the theoretical one ( $E_g^I = 1.46 \text{ eV}$ ) (Table I). Both  $E_g^D$  and  $E_g^I$  of  $\text{Pd}_3\text{P}_2(\text{S}_{1-x}\text{Se}_x)_8$  decrease monotonically with increasing  $x$  [Fig. 1(f)]. This is in line with the color changes of single crystals from red orange to dark red with Se doping.

Theoretical calculations confirm the increased lattice parameters and decreased band gaps of  $\text{Pd}_3\text{P}_2(\text{S}_{1-x}\text{Se}_x)_8$  with Se doping (Table I). To mimic the structure of

TABLE I. The calculated lattice constants (in units of  $\text{\AA}$ ), indirect band gap  $E_g^I$  (in units of eV), and bandwidth (BW, in units of meV) of  $\text{Pd}_3\text{P}_2\text{S}_8$ ,  $\text{Pd}_3\text{P}_2(\text{S}_{0.75}\text{Se}_{0.25})_8$ , and  $\text{Pd}_3\text{P}_2\text{Se}_8$  along with the experimental lattice constants.

		Expt.		Calc.			
		$a$	$c$	$a$	$c$	$E_g^I$	BW
$\text{Pd}_3\text{P}_2\text{S}_8$	bulk	6.842	7.247	6.918	7.314	1.46	348
	monolayer			7.115		1.85	68
P-1	bulk	6.930	7.283	6.960	7.491	1.09	325
	monolayer			7.138		1.69	69
P-2	bulk	6.930	7.283	6.991	7.354	1.36	403
	monolayer			7.192		1.72	69
$\text{Pd}_3\text{P}_2\text{Se}_8$	bulk			7.184	7.666	0.89	478
	monolayer			7.385		1.47	172

$\text{Pd}_3\text{P}_2(\text{S}_{0.75}\text{Se}_{0.25})_8$ , two typical structural configurations, namely P-1 with Se atoms at the S1 site (P-1 phase) and P-2 with Se atoms at the S2 site (P-2 phase), are considered [Fig. S1 in the supplemental material (SM)] [49]. The calculated total energy of the P-1 phase is  $363.2 \text{ meV/f.u.}$  lower than that of the P-2 phase for  $\text{Pd}_3\text{P}_2(\text{S}_{0.75}\text{Se}_{0.25})_8$ . This indicates that Se atoms prefer to dope into the S1 site, which may result from the longer bond length and weaker binding strength of the P-S1 bond than those of the P-S2 bond. The calculated lattice parameters of hypothetical  $\text{Pd}_3\text{P}_2\text{Se}_8$  are larger than those of  $\text{Pd}_3\text{P}_2\text{S}_8$  due to the larger ionic radius of  $\text{Se}^{2-}$  than  $\text{S}^{2-}$ . Meanwhile, the theoretical value of  $E_g^I$  of  $\text{Pd}_3\text{P}_2\text{Se}_8$  is also smaller than that of  $\text{Pd}_3\text{P}_2\text{S}_8$  (Table I), consistent with the experimental trend [Fig. 1(d)].

To understand the evolutions of the band gap and FB of  $\text{Pd}_3\text{P}_2(\text{S}_{1-x}\text{Se}_x)_8$  with Se doping, we first study the electronic structures of bulk  $\text{Pd}_3\text{P}_2\text{S}_8$ . Even with the three-dimensional structural features and the contributions of multiple orbitals from Pd, P, and S atoms, some of the unique features of the 2D kagome lattice of Pd can still be observed in  $\text{Pd}_3\text{P}_2\text{S}_8$ , including the FB centered just below the Fermi level  $E_F$  and the Dirac point at the  $K$  point of the Brillouin zone [Fig. 2(a)]. From the partial density of states (PDOS), it can be seen that the valance bands near  $E_F$  mainly consist of Pd- $d$  and S- $p$  orbitals, while the P orbitals are far away from  $E_F$ . The common peaks of Pd- $d$  and S- $p$  PDOSs indicate the presence of  $p$ - $d$  hybridizations. These  $p$ - $d$  hybridizations vied for influence and dominance below  $-0.28 \text{ eV}$ , while for the FBs it mainly depends on Pd- $d$  orbitals. In comparison with other kagome materials,  $\text{Pd}_3\text{P}_2\text{S}_8$  has a FB with a rather small BW ( $348 \text{ meV}$ ) (Table I). To explore its origin, we calculate the integrated charge densities (ICDs) of FBs for bulk  $\text{Pd}_3\text{P}_2\text{S}_8$  with the local Cartesian coordinates, whose axes are along the Pd-S bonds and perpendicular to the  $\text{PdS}_4$  square plane [Figs. 1(a) and 2(b)]. Interestingly, the FB exhibits a nearly single-orbital (Pd- $d_{z^2}$ -like orbital) behavior with the direction perpendicular to the  $\text{PdS}_4$  square plane. Actually, this can be well explained by the splitting of the energy level of a  $\text{Pd}^{2+}$  ion in the local square-planar crystal field [Fig. 2(e)], similar to the case of  $\text{NdNiO}_2$  [53]. The topmost occupied orbital of a  $\text{Pd}^{2+}$  ion is  $d_{z^2}$ , and this is consistent with the PDOS shown in Fig. 2(a). In addition, the bands just below the FB consist mainly of

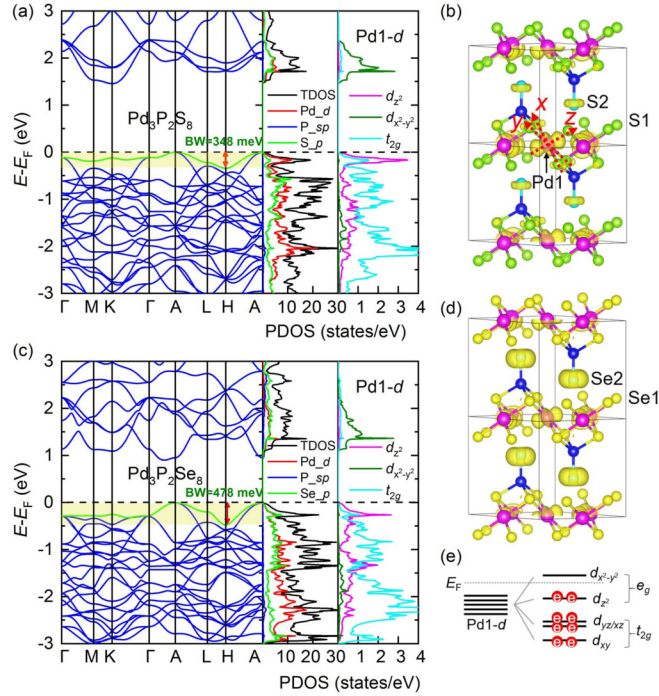


FIG. 2. Band structures, total density of states (TDOS), and PDOS of Pd- $d$ , P- $sp$ , and S(Se)- $p$  orbitals for bulk (a)  $\text{Pd}_3\text{P}_2\text{S}_8$  and (c)  $\text{Pd}_3\text{P}_2\text{Se}_8$ . The BWs are marked in green. (b),(d) The ICDs of flat bands for bulk  $\text{Pd}_3\text{P}_2\text{S}_8$  and  $\text{Pd}_3\text{P}_2\text{Se}_8$ , respectively. The isosurface of charge densities is set to  $0.003 e/\text{\AA}^3$ . (e) Schematic diagram of crystal field splitting for the Pd1 atom.

Pd- $t_{2g}$  (nondegenerate  $d_{xy}$  and doubly degenerate  $d_{yz}/d_{xz}$ ) orbitals and S- $p$  orbitals [Fig. 2(a)]. This  $p$ - $d$  hybridization results in the large dispersion of these bands. In contrast, because of the large distance between the Pd atom and the S2 atoms in the neighboring layers, the electron hopping perpendicular to the  $\text{PdS}_4$  square plane is limited and there is only a small amount of charges around S2 atoms contributing to the FB [Fig. 2(b)], giving rise to the small BW of FB. In fact, a similar phenomenon is also observed at the surface of the kagome metal FeSn by destructing electronic hopping along the vertical direction [54].

Considering Se doping, the main features of the electronic structure of bulk  $\text{Pd}_3\text{P}_2(\text{S}_{1-x}\text{Se}_x)_8$  ( $x = 0.25$  and 1) [Fig. 2(c) and Fig. S2 in the SM] are similar to that of  $\text{Pd}_3\text{P}_2\text{S}_8$  [49]. But the weight of Se- $p$  orbitals below the  $E_F$  in  $\text{Pd}_3\text{P}_2\text{Se}_8$  is larger than that of S- $p$  orbitals in  $\text{Pd}_3\text{P}_2\text{S}_8$  [Figs. 2(a) and 2(c)], suggesting the stronger  $p$ - $d$  hybridizations in the former. Meanwhile, the BW of FB (478 meV) (Table I) and the ICDs around Se2 in  $\text{Pd}_3\text{P}_2\text{Se}_8$  are also larger than those of  $\text{Pd}_3\text{P}_2\text{S}_8$  [Figs. 2(b) and 2(d)]. Furthermore, the FB of the P-2 phase exhibits a larger dispersion along the  $\Gamma$ -A direction than that of the P-1 phase (Table I and Fig. S2 in the SM) [49]. This large dispersion can also partially explain the reduced  $E_g^1$  with Se doping, especially at the S2 site [Fig. 1(f) and Table I]. The above results clearly indicate that with increasing Se content, the increase of Pd-Ch (Ch = S, Se)  $p$ - $d$  hybridization, especially when the Se atoms are located at apical sites, has a significant influence on interlayer coupling, the BW of the

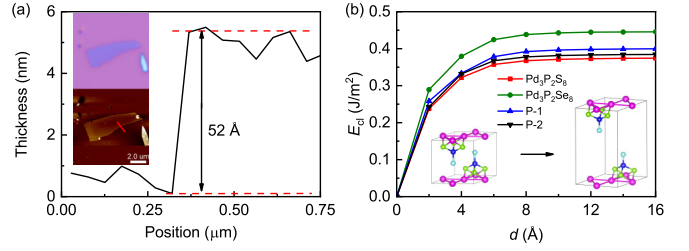


FIG. 3. (a) Height profile across the sample edge along the direction shown by the arrow in the lower inset. Upper and lower insets show the optical and AFM images of a cleaved thin flake of  $\text{Pd}_3\text{P}_2\text{S}_8$  crystal. The bar in the lower inset is  $2 \mu\text{m}$ . (b) Calculated cleavage energies  $E_{cl}$  as a function of  $d$  for  $\text{Pd}_3\text{P}_2\text{S}_8$ ,  $\text{Pd}_3\text{P}_2\text{Se}_8$ , as well as  $\text{Pd}_3\text{P}_2(\text{S}_{0.75}\text{Se}_{0.25})_8$  with P-1 and P-2 configurations.

FB, and the band gap, which seems to hinder realization of the ultra-FB of the Pd kagome lattice.

To reduce the interlayer coupling, a natural idea is to exfoliate the layered compounds of  $\text{Pd}_3\text{P}_2\text{Ch}_8$  down to monolayers. Previous experiment reported that  $\text{Pd}_3\text{P}_2\text{S}_8$  can be easily cleaved down to a few layers or even a monolayer [38]. For the whole series of  $\text{Pd}_3\text{P}_2\text{Ch}_8$  crystals, they are also easy to exfoliate to a few layers like  $\text{Pd}_3\text{P}_2\text{S}_8$ . Here, we take  $\text{Pd}_3\text{P}_2\text{S}_8$  as an example for cleavage. The step height across an edge of the cleaved sample [red line in the lower inset of Fig. 3(a)] is  $52 \text{\AA}$  [Fig. 3(a)], which is about 7 unit cells of  $\text{Pd}_3\text{P}_2\text{S}_8$ . Moreover, the rather large area of exfoliated thin flakes with the same color ( $\sim 7 \times 3 \mu\text{m}^2$ ) suggests a uniform thickness through the whole sample [upper inset of Fig. 3(a)]. It is noted that the thin flakes of  $\text{Pd}_3\text{P}_2\text{Ch}_8$  are stable in air without a color change for several days. To reveal the evolution of interlayer coupling strength with Se doping further, the cleavage energies  $E_{cl}$  are calculated by increasing interlayer distance  $d$  [inset of Fig. 3(b)]. The  $E_{cl}$  increases quickly with increasing  $d$  and then converges to the saturation value of  $0.37 \text{ J/m}^2$  ( $23 \text{ meV/\AA}^2$ ) when  $d$  is larger than  $\sim 8 \text{\AA}$ . With Se doping, the  $E_{cl}$  increases gradually and reaches  $0.45 \text{ J/m}^2$  ( $28 \text{ meV/\AA}^2$ ) for hypothetical  $\text{Pd}_3\text{P}_2\text{Se}_8$ . In addition, the P-1 phase has a slightly larger  $E_{cl} = 0.40 \text{ J/m}^2$  than the P-2 phase ( $E_{cl} \sim 0.38 \text{ J/m}^2$ ). These results confirm the significant influence of chalcogen atoms at the apical site on the strength of interlayer coupling. Although the  $E_{cl}$  increases with Se doping, they are still comparable with those values for most of the well-known vdW materials, like graphite and  $\text{MoS}_2$  ( $E_{cl} = 13\text{--}21 \text{ meV/\AA}^2$ ) [51]. Thus  $\text{Pd}_3\text{P}_2\text{Ch}_8$  can be classified into the group of easily exfoliable materials ( $E_{cl} < 35 \text{ meV/\AA}^2$ ) [52], even though they have the wavy structure of Pd-P-Ch layers.

The feasible cleavage of  $\text{Pd}_3\text{P}_2\text{Ch}_8$  down to atomically thin films or even a monolayer alters the interlayer coupling and also has a significant influence on its electronic structure. To further clarify the evolution of FBs with the strength of interlayer interaction, we consider the continuous evolution of the band structure in bilayers  $\text{Pd}_3\text{P}_2\text{S}_8$  with the variation of interlayer spacing  $\Delta d = (d - d_{\text{Bulk}})$ , where  $d_{\text{Bulk}}$  is the interlayer distance in bulk materials [Fig. 4(a)]. When  $\Delta d = 0$ , the strong interlayer interaction leads to the coupling of two sets of FBs derived from two different layers with relatively large BW (212 meV). It is noted that this value is close to

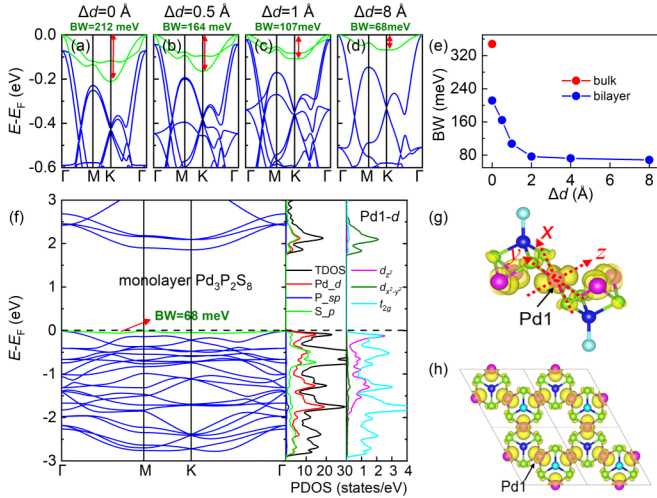


FIG. 4. (a)–(d) Band structures of the bilayer  $\text{Pd}_3\text{P}_2\text{S}_8$  with increasing  $\Delta d$ . The green bands mark the two FBs. (e) The BW of two FBs as a function of  $\Delta d$ , as well as the value of bulk  $\text{Pd}_3\text{P}_2\text{S}_8$  (red dot). (f) Band structure, TDOS, and PDOS of Pd- $d$ , P- $sp$ , and S- $p$  orbitals for monolayer  $\text{Pd}_3\text{P}_2\text{S}_8$ . (g) Side view and (h) top view of the ICDs of FB for the monolayer  $\text{Pd}_3\text{P}_2\text{S}_8$ .

the average value of bulk and monolayer  $\text{Pd}_3\text{P}_2\text{S}_8$  (Table I) possibly because in the bilayer case almost half of the interlayer couplings are absent when compared to the bulk one. With increasing  $\Delta d$ , the weakened coupling of two sets of FBs narrows the BW [Figs. 4(b) and 4(c)]. Finally, when  $\Delta d$  is large enough ( $\Delta d = 8 \text{ \AA}$ ), the interlayer coupling becomes negligible and the two sets of FBs are almost degenerated [Fig. 4(d)]. Correspondingly, the BW of two FBs decreases more than threefold [Fig. 4(e)]. If exfoliated to a monolayer, the Pd-S2 distance becomes infinite and the charge around S2 atoms vanishes [Figs. 4(g) and 4(h)], suggesting a lack of interlayer electron hopping along the out-of-plane direction. As a result, the much narrower BW of the FB ( $\sim 68 \text{ meV}$ ) appears in the monolayer of  $\text{Pd}_3\text{P}_2\text{S}_8$  [Fig. 4(f)]. On the other hand, the BW of the FB for monolayer  $\text{Pd}_3\text{P}_2\text{Se}_8$  is slightly larger than that of monolayer  $\text{Pd}_3\text{P}_2\text{S}_8$ , and the ICDs near Se1 are also larger than that of S1 in  $\text{Pd}_3\text{P}_2\text{S}_8$  (Fig. S3 in the SM) [49]. This suggests that the increased intralayer coupling between Pd and Se1 due to stronger  $p$ - $d$  hybridization is also unfavorable for the flatness of FB. We have also calculated the

band structures of  $\text{Pd}_3\text{P}_2\text{Ch}_8$  with spin-orbit coupling (Fig. S4 in SM) [49]. The spin-orbit coupling has a minor effect on the band structures. In addition, the magnetic calculations suggest that the ground states of these materials are nonmagnetic, which is consistent with the low spin state of  $\text{Pd}^{2+}$  ions ( $S = 0$ ).

#### IV. CONCLUSION

In summary, we study the doping effects of Se on the vdW kagome semiconductor  $\text{Pd}_3\text{P}_2\text{S}_8$  single crystals. It is found that with Se doping, the lattice parameters increase but the band gaps  $E_g$  decrease monotonically, which is related to the increased dispersion of FB near  $E_F$  because of the enhanced interlayer coupling due to Se doping, especially when Se atoms occupy the apical sites of  $\text{PCh}_4$  tetrahedra. In contrast, once such interlayer coupling is eliminated in monolayer  $\text{Pd}_3\text{P}_2\text{Ch}_8$ , an unusual ultra-FB of a Pd kagome lattice with narrow BW can be formed. This ultra-FB not only roots in the kagome structure of  $\text{Pd}_3\text{P}_2\text{Ch}_8$  but also is closely related to the unique square planar crystal field of  $\text{PdCh}_4$  with a  $\text{Pd}^{2+}$  ion in a  $4d^8$  configuration. The latter isolates the  $d_{z^2}$  band from other  $d$  bands of the  $\text{Pd}^{2+}$  ion when the interlayer electron hopping perpendicular to the  $\text{PdCh}_4$  square plane is suppressed in the 2D limit. Thus,  $\text{Pd}_3\text{P}_2\text{Ch}_8$  provides a unique platform to study the physics of FB in a kagome lattice.

#### ACKNOWLEDGMENTS

This work was supported by National Key R&D Program of China (Grants No. 2018YFE0202600, No. 2017YFA0302903, and No. 2019YFA0308603), Beijing Natural Science Foundation (Grant No. Z200005), National Natural Science Foundation of China (Grants No. 12174443, No. 11934020, and No. 62175210), the Fundamental Research Funds for the Central Universities and Research Funds of Renmin University of China (RUC) (Grants No. 18XNLG14, No. 19XNLG13, and No. 19XNLG17), and Beijing National Laboratory for Condensed Matter Physics. Computational resources were provided by the Physical Laboratory of High-Performance Computing at Renmin University of China.

[1] D. Leykam, A. Andreanov, and S. Flach, *Adv. Phys.* **X 3**, 1473052 (2018)  
 [2] J.-W. Rhim and B.-J. Yang, *Adv. Phys.* **X 6**, 1901606 (2021).  
 [3] Z. Liu, F. Liu, and Y.-S. Wu, *Chin. Phys. B* **23**, 077308 (2014).  
 [4] A. Mielke, *J. Phys. A* **24**, 3311 (1991).  
 [5] H. Tasaki, *Prog. Theor. Phys.* **99**, 489 (1998).  
 [6] S. Miyahara, S. Kusuta, and N. Furukawa, *Physica C* **460-462**, 1145 (2007).  
 [7] W.-H. Ko, P. A. Lee, and X.-G. Wen, *Phys. Rev. B* **79**, 214502 (2009).  
 [8] C. Wu, D. Bergman, L. Balents, and S. Das Sarma, *Phys. Rev. Lett.* **99**, 070401 (2007).

[9] B. Jaworowski, A. D. Güçlü, P. Kaczmarkiewicz, M. Kupczyński, P. Potasz, and A. Wójs, *New J. Phys.* **20**, 063023 (2018).  
 [10] K. Ohgushi, S. Murakami, and N. Nagaosa, *Phys. Rev. B* **62**, R6065 (2000).  
 [11] E. Tang, J.-W. Mei, and X.-G. Wen, *Phys. Rev. Lett.* **106**, 236802 (2011).  
 [12] A. Mielke, *J. Phys. A* **24**, L73 (1991).  
 [13] A. Mielke, *J. Phys. A* **25**, 4335 (1992).  
 [14] B. Sutherland, *Phys. Rev. B* **34**, 5208 (1986).  
 [15] E. H. Lieb, *Phys. Rev. Lett.* **62**, 1201 (1989).  
 [16] H. Tasaki, *Phys. Rev. Lett.* **69**, 1608 (1992).

- [17] C. Wu and S. Das Sarma, *Phys. Rev. B* **77**, 235107 (2008).
- [18] Z. Liu, Z. F. Wang, J. W. Mei, Y. S. Wu, and F. Liu, *Phys. Rev. Lett.* **110**, 106804 (2013).
- [19] S.-L. Yu and J.-X. Li, *Phys. Rev. B* **85**, 144402 (2012).
- [20] W.-S. Wang, Z.-Z. Li, Y.-Y. Xiang, and Q.-H. Wang, *Phys. Rev. B* **87**, 115135 (2013).
- [21] M. L. Kiesel, C. Platt, and R. Thomale, *Phys. Rev. Lett.* **110**, 126405 (2013).
- [22] L. Balents, *Nature (London)* **464**, 199 (2010).
- [23] L. Ye, M. Kang, J. Liu, F. von Cube, C. R. Wicker, T. Suzuki, C. Jozwiak, A. Bostwick, E. Rotenberg, D. C. Bell, L. Fu, R. Comin, and J. G. Checkelsky, *Nature (London)* **555**, 638 (2018).
- [24] Z. Lin, J.-H. Choi, Q. Zhang, W. Qin, S. Yi, P. Wang, L. Li, Y. Wang, H. Zhang, Z. Sun, L. Wei, S. Zhang, T. Guo, Q. Lu, J.-H. Cho, C. Zeng, and Z. Zhang, *Phys. Rev. Lett.* **121**, 096401 (2018).
- [25] Z. Liu, M. Li, Q. Wang, G. Wang, C. Wen, K. Jiang, X. Lu, S. Yan, Y. Huang, D. Shen, J.-X. Yin, Z. Wang, Z. Yin, H. Lei, and S. Wang, *Nat. Commun.* **11**, 4002 (2020).
- [26] M. Kang, S. Fang, L. Ye, H. C. Po, J. Denlinger, C. Jozwiak, A. Bostwick, E. Rotenberg, E. Kaxiras, J. G. Checkelsky, and R. Comin, *Nat. Commun.* **11**, 4004 (2020).
- [27] M. Li, Q. Wang, G. Wang, Z. Yuan, W. Song, R. Lou, Z. Liu, Y. Huang, Z. Liu, H. Lei, Z. Yin, and S. Wang, *Nat. Commun.* **12**, 3129 (2021).
- [28] T.-H. Han, J. S. Helton, S. Chu, D. G. Nocera, J. A. Rodriguez-Rivera, C. Broholm, and Y. S. Lee, *Nature (London)* **492**, 406 (2012).
- [29] S. Nakatsuji, N. Kiyohara, and T. Higo, *Nature (London)* **527**, 212 (2015).
- [30] E. Liu, Y. Sun, N. Kumar, L. Muechler, A. Sun, L. Jiao, S.-Y. Yang, D. Liu, A. Liang, Q. Xu, J. Kroder, V. Süß, H. Borrmann, C. Shekhar, Z. Wang, C. Xi, W. Wang, W. Schnelle, S. Wirth, Y. Chen *et al.*, *Nat. Phys.* **14**, 1125 (2018).
- [31] Q. Wang, Y. Xu, R. Lou, Z. Liu, M. Li, Y. Huang, D. Shen, H. Weng, S. Wang, and H. Lei, *Nat. Commun.* **9**, 3681 (2018).
- [32] J.-X. Yin, S. S. Zhang, H. Li, K. Jiang, G. Chang, B. Zhang, B. Lian, C. Xiang, I. Belopolski, H. Zheng, T. A. Cochran, S.-Y. Xu, G. Bian, K. Liu, T.-R. Chang, H. Lin, Z.-Y. Lu, Z. Wang, S. Jia, W. Wang *et al.*, *Nature (London)* **562**, 91 (2018).
- [33] J.-X. Yin, S. S. Zhang, G. Chang, Q. Wang, S. S. Tsirkin, Z. Guguchia, B. Lian, H. Zhou, K. Jiang, I. Belopolski, N. Shumiya, D. Multer, M. Litskevich, T. A. Cochran, H. Lin, Z. Wang, T. Neupert, S. Jia, H. Lei, and M. Z. Hasan, *Nat. Phys.* **15**, 443 (2019).
- [34] J.-X. Yin, W. Ma, T. A. Cochran, X. Xu, S. S. Zhang, H.-J. Tien, N. Shumiya, G. Cheng, K. Jiang, B. Lian, Z. Song, G. Chang, I. Belopolski, D. Multer, M. Litskevich, Z.-J. Cheng, X. P. Yang, B. Swidler, H. Zhou, H. Lin *et al.*, *Nature (London)* **583**, 533 (2020).
- [35] B. R. Ortiz, S. M. L. Teicher, Y. Hu, J. L. Zuo, P. M. Sarte, E. C. Schueller, A. M. M. Abeykoon, M. J. Krogstad, S. Rosenkranz, R. Osborn, R. Seshadri, L. Balents, J. He, and S. D. Wilson, *Phys. Rev. Lett.* **125**, 247002 (2020).
- [36] B. R. Ortiz, P. M. Sarte, E. M. Kenney, M. J. Graf, S. M. L. Teicher, R. Seshadri, and S. D. Wilson, *Phys. Rev. Materials* **5**, 034801 (2021).
- [37] Q. Yin, Z. Tu, C. Gong, Y. Fu, S. Yan, and H. Lei, *Chin. Phys. Lett.* **38**, 037403 (2021).
- [38] S. Park, S. Kang, H. Kim, K. H. Lee, P. Kim, S. Sim, N. Lee, B. Karuppannan, J. Kim, J. Kim, K. I. Sim, M. J. Coak, Y. Noda, C. H. Park, J. H. Kim, and J. G. Park, *Sci. Rep.* **10**, 20998 (2020).
- [39] P. E. Blöchl, *Phys. Rev. B* **50**, 17953 (1994).
- [40] G. Kresse and D. Joubert, *Phys. Rev. B* **59**, 1758 (1999).
- [41] G. Kresse and J. Hafner, *Phys. Rev. B* **47**, 558 (1993).
- [42] G. Kresse and J. Furthmüller, *Comput. Mater. Sci.* **6**, 15 (1996).
- [43] G. Kresse and J. Furthmüller, *Phys. Rev. B* **54**, 11169 (1996).
- [44] J. P. Perdew, K. Burke, and M. Ernzerhof, *Phys. Rev. Lett.* **77**, 3865 (1996).
- [45] S. Grimme, J. Antony, S. Ehrlich, and S. Krieg, *J. Chem. Phys.* **132**, 154104 (2010).
- [46] J. P. Perdew, A. Ruzsinszky, J. Tao, V. N. Staroverov, G. E. Scuseria, and G. I. Csonka, *J. Chem. Phys.* **123**, 062201 (2005).
- [47] T. A. Bither, P. C. Donohue, and H. S. Young, *J. Solid State Chem.* **3**, 300 (1971).
- [48] A. Simon, K. Peters, E. M. Peters, and H. Hahn, *Z. Naturforsch. B* **38**, 426 (1983).
- [49] See Supplemental Material at <http://link.aps.org/supplemental/10.1103/PhysRevB.105.155115> for the theoretical crystal structure of  $\text{Pd}_3\text{P}_2(\text{S}_{0.75}\text{Se}_{0.25})_8$ , the band structures, TDOS, and PDOS of Pd-*d*, P-*sp*, and S-*p* orbitals for bulk and monolayer  $\text{Pd}_3\text{P}_2(\text{S}_{0.75}\text{Se}_{0.25})_8$  with P-1 and P-2 configurations and  $\text{Pd}_3\text{P}_2\text{Ch}_8$ .
- [50] J. Tauc, R. Grigorovici, and A. Vancu, *Phys. Status Solidi B* **15**, 627 (1966).
- [51] T. Björkman, A. Gulans, A. V. Krasheninnikov, and R. M. Nieminen, *Phys. Rev. Lett.* **108**, 235502 (2012).
- [52] N. Mounet, M. Gibertini, P. Schwaller, D. Campi, A. Merkys, A. Marrazzo, T. Sohier, I. E. Castelli, A. Cepellotti, G. Pizzi, and N. Marzari, *Nat. Nanotechnol.* **13**, 246 (2018).
- [53] P. Jiang, L. Si, Z. Liao, and Z. Zhong, *Phys. Rev. B* **100**, 201106(R) (2019).
- [54] M. Han, H. Inoue, S. Fang, C. John, L. Ye, M. K. Chan, D. Graf, T. Suzuki, M. P. Ghimire, W. J. Cho, E. Kaxiras, and J. G. Checkelsky, *Nat. Commun.* **12**, 5345 (2021).